Nanoscale

PAPER

View Article Online
View Journal | View Issue



Cite this: *Nanoscale*, 2025, **17**, 27959

# Serum albumin-coated stellate mesoporous silica nanocomposites inhibit metastatic outgrowth in zebrafish embryos

Nandini Asokan, [a,b,c,d,h] Vincent Mittelheisser,[a,b,c,d] Arnaud Jablonski,[e] Alexandre Adam, [e] Joëlle Bizeau, [e] Sébastien Harlepp,[a,b,c,d,f] Vincent Hyenne,[a,b,c,d] Olivier Lefebvre,*[a,b,c,d] Jacky G. Goetz, *[a,b,c,d] Mariana Tasso*[g] and Damien Mertz *[e]

Mesoporous silica-based nanoparticles (NPs) are promising tools for developing targeted therapeutic interventions in cancer. Endowed with a large pore silica shell suitable for drug encapsulation and with a responsive magnetic core, iron oxide stellate mesoporous silica (IO STMS) NPs stand out. However, their impact and potential toxicity on relevant *in vivo* models have not been carefully tested yet. Herein, we assessed the impact of these IO STMS nanocomposites in a syngeneic metastasis assay in zebrafish. NPs were surface-modified with human serum albumin (HSA) and loaded with or without chemotherapeutic doxorubicin (DOX). *In vitro*, DOX-loaded NPs were expectedly more toxic to zebrafish melanoma (Zmel) cells than NPs without DOX. In zebrafish embryos, the NPs were rapidly distributed through blood circulation and were found to colocalize over time with the vascular endothelium and local macrophages. Surprisingly, the NPs efficiently reduced the outgrowth of Zmel tumoral masses in an experimental metastasis assay in zebrafish embryos regardless of their loading with DOX. The anti-metastatic effect of these NPs was further improved by increasing the amount of HSA coating, resulting in higher embryo survival. Altogether, IO STMS NPs showed promising anti-cancer effects on a relevant zebrafish metastasis model, inhibiting metastatic outgrowth *in vivo* independently of the drug loading. This opens the door to further testing for better exploiting their targeting and drug delivery potentials.

Received 8th June 2025,
Accepted 28th October 2025

DOI: 10.1039/d5nr02444g

rsc.li/nanoscale



## Introduction

The application of nanotechnology in cancer medicine offers the possibility to improve the efficiency of current anti-cancer therapies. In recent years, a wide variety of new nanoparticles (NPs) have been designed for drug delivery, imaging and therapeutic purposes.[1,2] With successful lab-based and pre-clinical screenings for toxicity and functional efficacy, these nanoplatforms could improve the quality of life in cancer patients during treatment and along their life span. Of the myriad of NPs investigated in the past years, including soft polymers and lipid-based and inorganic nanoparticles, it has been reported that at least 80 NP-based therapies are under clinical investigation and 15 nanomedicines are currently approved.[3] However, among the main challenges to be solved, the design of nanomedicines with efficient targeting, controlled biodegradability, and favorable scaling-up, or the possibility to control drug delivery with local or remote stimuli, are the principal issues to resolve.

Regarding specifically silica-based nanoparticles, to date, there are mainly two theranostic nanoformulations used in clinical phases: Aurolase®, a silica core capped with a gold shell for near infrared light (NIR) treatment of prostate cancer, and Cornell dots®, which are small silica dots (~5 nm size) functionalised with an RGD peptide targeting ligand and a positron emission tomography (PET) probe for the detection of metastatic cancer.[4] To date, there is no mesoporous silica translation in the clinics while they have the advantage of drug

[a]*Tumor Biomechanics Lab, INSERM UMR-S1109, Strasbourg, France. E-mail: jacky.goetz@inserm.fr, lefebvre@unistra.fr*
[b]*Université de Strasbourg, Strasbourg, France*
[c]*Fédération de Médecine Translationnelle de Strasbourg (FMTS), Strasbourg, France*
[d]*Equipe Labellisée Ligue Contre le Cancer, Strasbourg, France*
[e]*Institut de Physique et Chimie des Matériaux de Strasbourg (IPCMS), UMR-7504 CNRS-Université de Strasbourg, France. E-mail: damien.mertz@ipcms.unistra.fr*
[f]*Institut de Cancérologie Strasbourg Europe, 67000 Strasbourg, France*
[g]*Institute of Nanosystems (INS), School of Bio and Nanotechnology, National University of San Martin – CONICET, Buenos Aires, Argentina. E-mail: mtasso@unsam.edu.ar*
[h]*Current address: University Hospital Tübingen and University Tübingen, Clinic for Internal Medicine II, Hematology, Oncology, Clinical Immunology & Rheumatology and Medical Faculty, Tübingen, Germany*

transport as compared to non-porous silica. Mesoporous silica nanoparticles (MSNs), with their unique properties to encapsulate small and large biomolecules (*e.g.* RNA and proteins), exhibit good biocompatibility and biodegradability, ensuring their promising use in drug delivery applications.[5] Various mild chemical methods allow for fine-tuning of their pore structure, for instance, by playing a role in the porogen surfactant length or in its counterion, enabling high versatility in drug loading or protein encapsulation.[6,7] Regarding their biodegradability, recent *in vitro* and *in vivo* (mouse) studies indicate that MSNs degrade in periods ranging from several days to several weeks and that the main factors governing degradation and clearance are the NP concentration, their degree of agglomeration and their pore size.[8] Moreover, the integration of a biocompatible inorganic core into such a silica structure to afford localized treatment (heating, formation of reactive oxygen species) under external fields (light, alternating magnetic field) appears as a very appealing approach for future treatments.

Using sol–gel techniques in the presence of biocompatible inorganic cores (such as iron oxide, IO), core–shell nanomaterials have been developed, integrating the combinatorial properties of both the core and shell within a single nanostructure. In this respect, we have recently developed a new generation of core–shell iron oxide MSNs featuring a silica shell of stellate morphology (STMS) and a controlled pore structure.[9] This stellate shell, formed in the presence of cetyltrimethylammonium tosylate (CTATos) surfactant as a dendritic pore-directing agent, is fully tunable and exhibits a surface area of approximately 500 $m^2$ $g^{-1}$ with a pore size ranging from 10 to 15 nm. These IO STMS NPs were efficient at inducing cancer cell death *in vitro* under magnetic hyperthermia and were shown to be potential diagnostic markers for fluorescence and magnetic resonance imaging.[10] Furthermore, when loaded with doxorubicin (DOX), these NPs behaved as effective drug carriers and as prospective photothermal agents.[11] However, to date, they have never been assessed in an *in vivo* model, which is the purpose of this work.

Another key aspect is the NP surface functionalization, as it will ultimately determine the NP interaction with the biological environment. The functionalization of MS with serum proteins such as human serum albumin (HSA) is usually reported as a way to improve the biocompatibility and to limit immunogenicity. Given the isoelectric point (IEP) of HSA at 4.7, it ensures satisfactory colloidal stability in physiological buffer and helps to increase the blood circulation time. Regarding drug delivery aspects, serum protein coating is also reported to control or prolong the drug release profiles *via* gate-keeping strategies. In particular, in this work, as detailed later in the manuscript, we used a strategy based on isobutyramide grafts to bind HSA at the mesoporous silica surface.

In recent years, zebrafish (*Danio rerio*) has rapidly become an established animal model system to study NPs.[12–18] The transparency of the zebrafish embryo allows for direct visualization of NP biodistribution and their interactions with host cells *in vivo*.[17,19] Furthermore, for a wide range of nanomaterials, recent studies indicate that NP behavior and the cellular uptake process are very similar between zebrafish and mammals.[20] Notably, the availability of fluorescent zebrafish reporter lines allows for the investigation of NP interactions with host cells, including endothelial cells and macrophages.[17,21,22] Besides, zebrafish xenograft models are very well established and have cancer avatars of different cancer cell types.[23–26] These models have been used for screening a large number of drugs and drug formulations for efficacy and toxicity.[26–28] Together with these characteristics, their low maintenance cost and amenability to high-throughput screens make the zebrafish embryo an ideal model for screening nanobiomaterial biodistribution, toxicity, bioaccumulation, and *in vivo* fate.[26–28]

To date, the vast majority of NP assessment studies on zebrafish focus only on toxicity.[29–33] Few studies have evaluated the toxicity of selected therapeutic MSNs in zebrafish[34–36] and their biodistribution and *in vivo* delivery potential.[37–39] NP distribution *in vivo* is highly influenced by endothelial cells, and only a few studies in zebrafish have demonstrated the active uptake of these NPs by endothelial cells.[17,20] Macrophages are another cell type that actively take up NPs, but NP uptake by macrophages has been shown to be inefficient for cancer therapy as it decreases the chances of NP accumulation at tumor sites.[40,41] In contrast, recent studies suggest that direct targeting of macrophages may be advantageous as these cells can be recruited to tumor sites.[42–44] Furthermore, among various drug formulations investigated in zebrafish for drug delivery against cancer, doxorubicin encapsulated with different nanocarriers in a zebrafish xenograft model has shown a reduction in tumor burden.[45–49] Further *in vivo* analysis of the dissemination, cellular uptake, toxicity and anti-metastatic behavior of IO STMS NPs is thus warranted.

In this work, we performed for the first time an *in vivo* study with core–shell IO STMS NPs. These NPs are well-characterized nanoplatforms that have superparamagnetic iron oxide cores and a versatile stellate mesoporous shell whose morphology and pore size can be tuned.[50] In these designs, the core–shell NPs were surface-modified with a tight HSA layer using isobutyramide (IBAM) grafts as efficient binders.[51] *In vivo*, the NP surface coverage with HSA is vital to limit NP opsonization while in circulation,[52,53] yet whether increasing HSA coverage provides any additional benefit remains to be tested. Herein, we exploited a syngeneic zebrafish melanoma model to study the impact of HSA-coated IO STMS NPs, loaded with or without DOX, on their anti-metastatic potential. While DOX loading provided a significant advantage in the cytotoxicity of Zmel cells *in vitro*, it had no impact when NPs were synchronously injected with metastatic cells *in vivo* in zebrafish embryos and their anti-metastatic potential was assessed. Yet, and interestingly, we report that NPs significantly reduced metastatic outgrowth and embryo survival, and that by increasing HSA coating, a further enhancement in tumor reduction and embryo survival was revealed.

 

## Materials and methods

### Chemicals

Tetraethyl orthosilicate (TEOS, ≥99.0%), cetyltrimethylammonium tosylate (CTATos, ≥98.0%), 2-amino-2-(hydroxymethyl)-1,3-propanediol (AHMPD, ≥99.9%), ammonium nitrate (NH4NO3), (3-amino propyl)triethoxysilane (APTES, 99%), isobutyryl chloride (IBC, 98%) and triethylamine (Et3N, ≥99%) were obtained from Sigma-Aldrich (France). Nitric acid (HNO3, 70%) and *N*,*N*-dimethylformamide (DMF, ≥99.9%) were purchased from Carlo-Erba. Iron(III) stearate (FeSt3) and fluorescein isothiocyanate (FITC) were obtained from TCI. Oleic acid (99%) was purchased from Alfa Aesar, while squalane (99%) was purchased from Acros Organic. Doxorubicin hydrochloride was obtained from OChem Inc. Human serum albumin (HSA) was purchased from Sigma Life Science. Dimethyl sulfoxide (DMSO) was obtained from Roth.

### Cell culture

DMEM, non-essential amino acids and 0.05% trypsin were obtained from Gibco. Fetal bovine serum (FBS), penicillin (50 units per mL) and streptomycin (50 μg $mL^{-1}$) were obtained from Thermo Fisher Scientific. 1-Phenyl-2-thiourea (PTU) and tricaine (ethyl-3-aminobenzoate-methanesulfonate) were obtained from Sigma-Aldrich.

### Synthesis of NPs and DOX loading

IBAM-modified IO@STMS NPs (IO@STMS@IBAM) were synthesized following a previously described procedure.[11] For drug loading, doxorubicin hydrochloride (DOX) (2 mg, 3.7 μmol) was dissolved in 1 mL of HEPES buffer (100 mM, pH = 7.5) and incubated with 2.5 mg of IO@STMS@IBAM NPs for 24 h on a stirring wheel at room temperature protected from light. The obtained IO@STMS@DOX NPs were collected by centrifugation (14 000*g*, 10 min) and washed three times with 4.5 mL of HEPES buffer (100 mM, pH = 7.5). The DOX concentration in the supernatants (after loading and washings) was measured by UV-Vis spectrophotometry to calculate the drug loading content (DLC) in the IO@STMS@DOX NPs. For this, a calibration curve of DOX in HEPES buffer (100 mM, pH = 7.5) was established by measuring the absorbance at 480 nm (Fig. S1E). According to this calibration curve, the molar extinction coefficient of DOX is 9772 $M^{-1}$ $cm^{-1}$. Finally, a DLC of 11.3%, meaning 113 μg of DOX per mg of NPs, was obtained and used for the whole biological study.

### FITC-labelling of HSA

The procedure was reported previously by Bizeau *et al.*[51] Briefly, a molar ratio of 2 FITC for 1 HSA protein was used to ensure efficient labelling. 5 mL of HSA solution (10 mg $mL^{-1}$) in $NaHCO_3$ buffer (0.1 mol $L^{-1}$, pH 8.5) was reacted with 59 μL of FITC solution (10 mg $mL^{-1}$ in DMSO) and stirred for 1 h. The mixture was protected from light during the whole procedure. After purification by dialysis against water (2 days, water was changed every 2 h), the final volume was measured to calculate the exact concentration. The HSA-FITC solution was aliquoted and stored at −20 °C for further use.

### HSA-FITC coating of the NPs

**HSA NPs.** NPs@HSA-FITC (and NPs@DOX@HSA-FITC) were prepared by dispersing 10 mg of IO@STMS@IBAM (and IO@STMS@IBAM@DOX) NPs in 2.5 mL of a solution of HSA-FITC (0.4 mg $mL^{-1}$ in 100 mM HEPES, pH 7.5), resulting in a 10 wt% HSA-FITC feed weight ratio. The coating was deposited by stirring the suspensions on a rotating wheel for 1 h, at room temperature and protected from light. The NPs@HSA-FITC (and NPs@DOX@HSA-FITC) were centrifuged (12 000*g*, 12 min) and washed twice (12 000*g*, 12 min) with HEPES buffer (100 mM, pH 7.5). These compounds are referred to as HSA NPs or HSA-Dox_NPs in the text.

**High HSA NPs.** For NPs@highHSA-FITC, an additional incubation with 1 mL of HSA-FITC at 10 mg $mL^{-1}$ (100% feed weight ratio) was performed to increase the protein surface coverage. For NPs@DOX@highHSA-FITC, additional successive incubations with 1 mL of HSA-FITC at 1 and 10 mg $mL^{-1}$ (10 and 100% feed weight ratios, respectively) were carried out to increase the protein surface coverage. High HSA NPs were therefore modified with a 110 wt% ratio of HSA, while DOX-containing high HSA NPs have a slightly higher exposure to HSA at a 120 wt%. As above, after HSA modification, the NPs were centrifuged (12 000*g*, 12 min) and washed twice (12 000*g*, 12 min) with HEPES buffer (100 mM, pH 7.5). These compounds are referred to as high HSA-NPs or high HSA-Dox_NPs in the text.

The surface contents of both HSA and high HSA were calculated from the measurement of the fluorescence emission intensity of the supernatants at 519 nm (excitation at 490 nm). The HSA-coated NPs (with and without DOX) were stored at 4 °C in 100 mM HEPES buffer at pH 7.5 at a high concentration (*i.e.*, in the mg $mL^{-1}$ range) prior to their use in the biological assays.

### Physicochemical characterization of the NPs

Once the IO@STMS NPs synthesized and the CTATos surfactant extracted from the pores, the NPs were imaged with a JEOL 2100 TEM instrument operating at 200 kV. Image J was used to analyse the size distribution of the NPs. IBAM graft density was evaluated using thermogravimetric analysis (TGA), which was performed using a STD Q600 (TA Instruments, 25–800 °C, a heating rate of 5 °C $min^{-1}$, and under an air flow rate of 50 mL $min^{-1}$). Hydrodynamic size distributions of the NPs with and without DOX, and at HSA and high HSA ratios, were evaluated by dynamic light scattering (DLS) in the intensity mode using a Malvern Nanosizer instrument operating at ambient temperature. Colloidal stability was evaluated in different buffers: HEPES (100 mM, pH 7.5), PBS (pH 7.4), and cell culture medium (RPMI).

### Cell culture

Zebrafish melanoma cells (Zmel-tdTomato) were cultured in DMEM containing 10% fetal bovine serum (FBS), 1% penicillin (50 units per mL), streptomycin (50 μg $mL^{-1}$) and 1% non-essential amino acids, and maintained at 28 °C in a humidified incubator supplied with 5% $CO_2$. The cells were harvested when reaching 85% confluence. The cells were detached with 0.05% trypsin and treated for 3 min at 28 °C.

### Cell viability

For cytotoxicity experiments, 125 000 Zmel-tdTomato were plated in a 24-well plate and incubated overnight. The day after, the medium was changed with media containing increasing concentrations (0–200 μg $mL^{-1}$) of NPs, doxorubicin-loaded NPs (Dox_NPs) or matching concentrations of doxorubicin HCl (DOX). These matching concentrations were calculated as NP concentration × 113 μg of DOX per mg NPs. The NPs were surface coated with HSA-FITC, as previously described. After 48 h, the cells were washed, fixed with PFA 4% and stained for 1 h with 2% crystal violet. Excess crystal violet was washed with tap water and plates were allowed to dry before imaging with an iBright 1500 imaging system. Images were loaded on ImageJ and the crystal violet mean grey intensity in each well was measured after oval selection definition.

### Cellular internalization *in vitro*

For internalization experiments, 500 000 Zmel-tdTomato cells were plated in a 4-well LabTek chamber and incubated overnight. The day after, the medium was changed with complete medium containing 100 μg $mL^{-1}$ of NPs or Dox_NPs. The NPs were surface coated with HSA-FITC, as previously described. After 5 h of incubation at 28 °C, the cells were washed and fixed with PFA 4% before mounting in Fluoromount/DAPI. Slides were imaged using a LSM800 Zeiss confocal microscope with a Plan Apo ×40 oil (NA 1.4) objective. The excitation wavelengths were 405 nm for DAPI, 488 nm for FITC, and 554 nm for tdTomato.

### Intravascular injection of NPs in zebrafish embryos

Zebrafish embryos were obtained from the following strains: wildtype-AB, Tg(Kdrl.hsa-HRAS:mCherry),[54] and Tg(mpeg1:Gal4 UAS:NTR-mCherry).[55,56] Embryos were maintained at 28 °C in Danieau 0.3× medium, supplemented with 1-phenyl-2-thiourea after 24 h post-fertilization (hpf). All injection experiments were carried out at 48 hpf and imaged between 48 hpf and 72 hpf. All animal procedures were performed in accordance with the French and European Union animal welfare guidelines and supervised by the local ethics committee (Animal facility #A6748233; APAFIS #2018092515234191). At 48 hpf, zebrafish embryos were dechorionated and mounted on a 0.8% low melting agarose pad containing 650 μM tricaine (ethyl-3-aminobenzoate-methanesulfonate). Embryos were injected intravascularly in the duct of Cuvier with 2 × 13.9 nL of NPs (with and without doxorubicin, at 0.5 mg $mL^{-1}$) with a Nanoject microinjector 2 (Drummond) under a M205 FA stereomicroscope (Leica), as described previously.[57,58] The total injected DOX amount is 1.57 ng for the Dox_NPs. The total injected mass is 13.9 ng for the NPs. The NPs were surface coated with HSA-FITC, as detailed above. At 3 hpi (hours post-injection) and 24 hpi, the injected embryos were imaged using an Olympus IXplore Spin inverted spinning-disk microscope at 30× with a 1.05 NA (silicone) objective focusing on the head and caudal hematopoietic tissue region (CHT) (488 nm laser at 2% for 100 ms/561 nm laser at 15% for 300 ms). Quantification of NP colocalization with endothelial cells and macrophages was performed using an in-house macro in ImageJ (Fiji). Embryo survival after NP administration was monitored every day until 4 dpi (days post-injection), with embryos screened for any phenotypic abnormalities. Percentage of embryo survival was plotted using a Kaplan–Meier curve. Pacemaker activity was measured by recording the heartbeat of the embryos as short time–lapses using a stereomicroscope (Leica M205 FA). Heartbeats were manually counted.

### Assessment of NP effect on the macrophage number and length of main vessels

Quantification of the macrophage number in the head and trunk regions was performed on processed single *Z* planes based on intensity thresholding using Cell Profiler. The intersomitic vessel (ISV) length was measured from the point where the ISV sprouts from the dorsal aorta up to the tip of the ISV using ImageJ. Similarly, the mesencephalic vein (MsV) length was measured from the point where the MsV extends from the dorsal side up to the tip of the MsV reaching artery using ImageJ.

### Tumor co-localization assay *in vivo*

This experiment was carried out with two types of NPs: NPs with HSA and high HSA surface content, both with and without encapsulated doxorubicin. In a typical experiment, about 200 zebrafish melanoma cells (Zmel-tdTomato = Zmel_tdT) were injected into the duct of Cuvier at 36 hpf on a wildtype AB embryo. Embryos properly grafted with zebrafish melanoma cells were divided into 3 groups. At 48 hpf, 2 × 13.9 nL of PBS, NPs or Dox_NPs at 0.5 mg $mL^{-1}$ were injected into the circulation of the larvae of the pre-divided groups. The NPs were surface coated with HSA-FITC, as previously described. At 3 hpi, 24 hpi and 4 dpi, injected embryos were imaged using spinning disk microscopy focusing on the caudal hematopoietic tissue region (CHT). The tumor volume at different time points was quantified with Imaris (interactive microscopy image analysis) software. Data were normalized according to the initial volume at 3 hpi for each embryo. Embryo survival was quantified at the defined time points.

### Colocalization analysis

Colocalization was analyzed on processed single *Z* planes (Despeckle and Gaussian blur filter in Fiji) based on intensity

 

thresholding using Cell Profiler. The areas of overlapping regions between NPs and tumor cells were quantified. The percentage of NP colocalization with the tumor cell was calculated as a ratio of the NP overlap area to the total area of NP objects, multiplied by 100.

### Statistical analysis

Statistical analysis was performed using GraphPad Prism (version 10.2). Normality of the data was confirmed using the Shapiro–Wilkinson test. According to the results, different statistical tests were used, as described in each specific section and in figure legends. For data that follow a Gaussian distribution, an unpaired *t* test was used; if not, a Mann–Whitney approach was applied. Two-way ANOVA analysis was applied to analyse tumor growth over time using the two-stage linear step-up post-test procedure of Benjamini, Krieger and Yekutiel. Survival was analyzed using the log-rank (Mantel–Cox) test with a Bonferroni post-test setting the number of comparisons, *k*, to 3. Violin plots are employed to present the data, with median and quartiles included in the plots. *p*-Values smaller than 0.05 were considered as statistically significant. * = $p < 0.05$, ** = $p < 0.01$, *** = $p < 0.001$, and **** = $p < 0.0001$.

## Results and discussion

### Synthesis and characterization of the HSA-coated NPs

The NPs surface-modified with human serum albumin (HSA), denoted HSA NPs, and loaded with or without doxorubicin (DOX) molecules, were synthesized as previously reported by Adam *et al.*[11] (see Scheme S1 for the whole chemical strategy). This previous work from our group focused on the evaluation of the photothermal properties of the core–shell NPs, and on their drug loading/release capabilities as a function of pH and surface chemistry. Here, the aim is to analyze this well-characterized and versatile nanosystem under *in vivo* conditions and blood circulation, and upon interaction with circulating tumor cells, macrophages and endothelial cells present in the vasculature. Briefly, the iron oxide (IO) cores were obtained by thermal decomposition, a method allowing a precise control over nanoparticle size and composition. Transmission electron microscopy (TEM) images indicate monodisperse spherical NPs with an average size distribution of 26.4 ± 3.4 nm, while X-ray diffraction (XRD) confirms the spinel phase structure ($Fe_{3-x}O_4$, Fig. S1A–C). The stellate mesoporous silica (STMS) shell was grown around the iron oxide cores using the sol–gel procedure in the presence of CTATos as a templating agent directing the stellate large pore morphology. Then, the surfactant was removed to free the pores and avoid any further release in biological media. TEM images confirm the synthesis of individual core–shell IO@STMS NPs having an average diameter of 119.7 ± 12 nm and optimal colloidal stability in ethanol, as determined by dynamic light scattering (DLS) (Fig. 1A–C). The specific surface area and average pore size were determined for these core–shell NPs, according to Bizeau *et al.*, and are of 333 $m^2\ g^{-1}$ and *ca.* 7.7 nm, respectively. Next, the surface was chemically modified in two steps with isobutyramide (IBAM) moieties covalently grafted at the extremities of condensed aminosiloxane groups (Fig. S1D, thermogravimetric analysis). Covalent aminosilane and IBAM modifications of the silica shell were followed by DOX loading and HSA immobilization, respectively. IBAM groups were previously reported as suitable binders for DOX loading (H-bonds and pi–pi stacking interactions) and HSA immobilization (tight H-bonds).[11] DOX loading was set here at one specific loading condition, ensuring a drug content of 113 μg DOX per mg of NPs for the whole biological study. The DOX content was calculated from supernatant analysis by UV-vis spectrophotometry using calibration curves in HEPES buffer (Fig. S1E). Then, NPs (loaded with or without DOX) were afterwards exposed to a human serum albumin protein (HSA) solution at a 10 wt% ratio relative to the NP mass, giving rise to an HSA content on the NP surface of 96 μg HSA per mg of NPs. The HSA-FITC contents adsorbed on the NPs were calculated from supernatant analysis by fluorescence spectroscopy using a calibration curve in HEPES buffer (Fig. S1F). This weigh ratio ensured an excellent yield (close to 100% impregnation) and the possibility of DOX release at pH-mimicking intracellular conditions (~5.5) with a great efficiency.[11] Furthermore, an HSA coating in the range of 100–200 μg HSA per mg ensured HSA NP interactions with HeLa cancer cells with suitable cell uptake (at NP concentrations in cell culture <30 μg $mL^{-1}$).[10] TEM images in the work of Perton *et al.* previously illustrated the deposition of HSA onto the core–shell NPs and provide a clear evidence of the HSA surface modification.[10] *Z* potential values of these NPs were thoroughly analyzed in previous works from our team, resulting in a ZP between −20 and −25 mV at pH 7.5 (HEPES buffer) for the HSA-coated NPs without DOX,[10] and in a ZP of *ca.* −5 mV for the DOX and HSA-containing NPs.[11] Next, the colloidal stability of the NPs was evaluated in different biological media. Dynamic light scattering (DLS) measurements in RPMI cell culture medium provided an average HSA NP diameter of 234 ± 4 nm (DLS *Z*-average value), with good colloidal stability. On the other hand, NPs tended to form aggregates of micron size in buffers such as HEPES or PBS. For the DOX-loaded NPs, the results are presented in Fig. 1D–F, while the whole study with and without DOX is presented in Fig. S2 with the same conclusions.

### Drug-loaded HSA NPs are cytotoxic to zebrafish melanoma cells *in vitro* but not HSA NPs

We first assessed the impact of these engineered NPs on a relevant metastatic melanoma model (Zmel) that is compatible with the syngeneic experimental metastasis assays to be implemented further. For that, we evaluated the viability of Zmel cells (engineered to express the fluorescent TdTomato protein, named Zmel_tdT) upon 48 hours exposure to various concentrations of the HSA NPs, loaded with or without DOX (Dox_NPs), and the drug DOX alone. The toxicity of Dox_NPs with respect to Zmel cells mirrored the one obtained with free DOX and scaled with increasing concentrations (Fig. 2A).

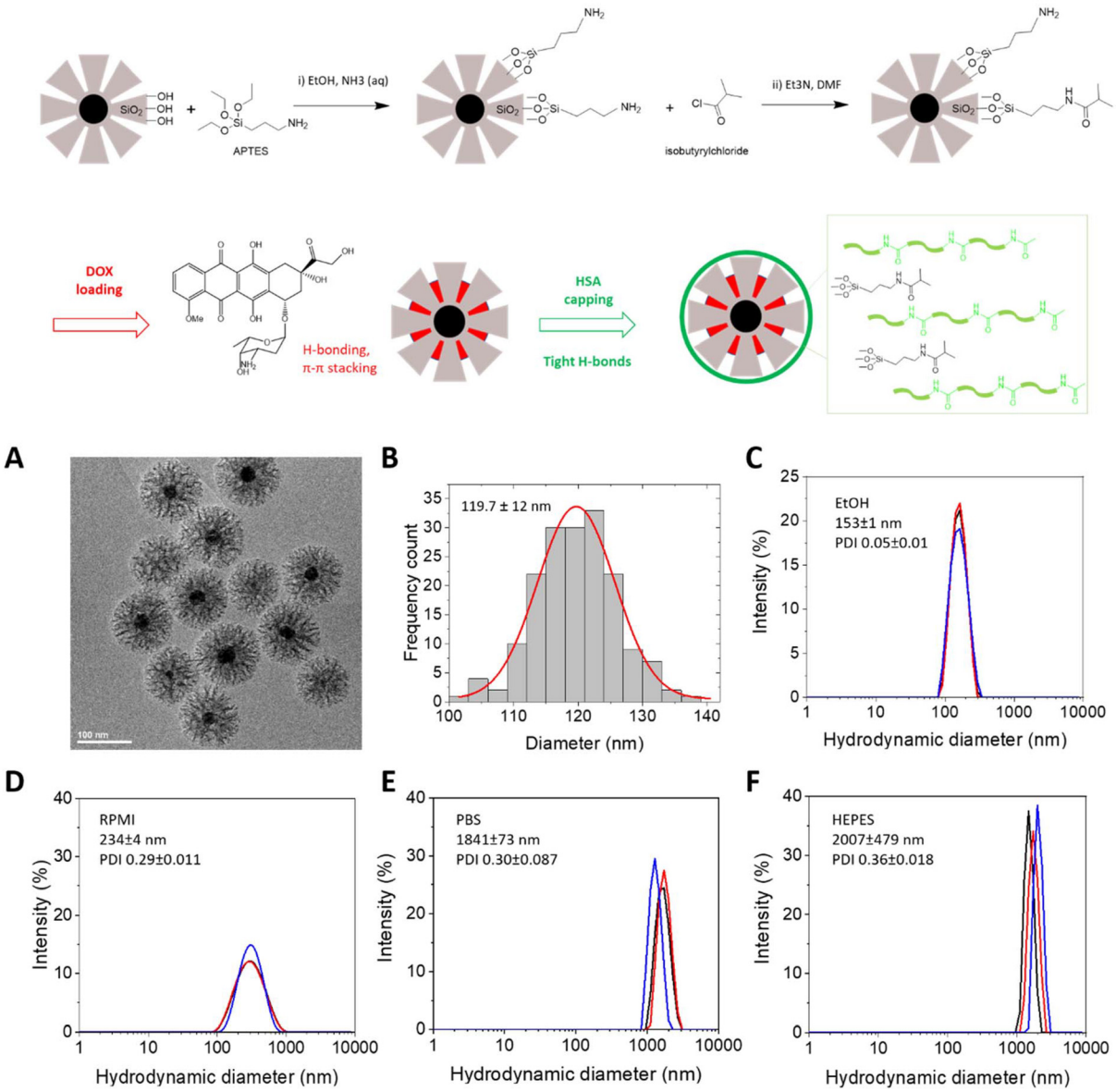


**Fig. 1** Main physicochemical features of the core–shell NPs surface-modified with HSA. Top: summary of the chemical steps, with initial silica shell modification with IBAM functional units, followed by doxorubicin (DOX) loading and final HSA surface immobilization. (A) TEM image of the core–shell NPs formed by an iron oxide core and a stellate mesoporous silica shell. (B) Associated NP size histogram. (C) Hydrodynamic size distribution of NPs in the storage solvent ethanol prior to DOX loading and HSA modification (DLS measurement). (D–F) Hydrodynamic size distribution of NPs in three different biological media (RPMI cell culture medium, PBS, and HEPES) for the core–shell NPs loaded with DOX and having HSA coating (DLS measurement). DLS runs were performed in triplicate in each medium as indicated in the DLS graphs. The average hydrodynamic diameter of the NP distribution is indicated as an inset. DLS = dynamic light scattering. PDI = polydispersity index.

Nevertheless, free DOX outweighs the encapsulated DOX in terms of cell viability losses, especially at low NP concentrations. Of note, high concentrations (above 50 μg $mL^{-1}$) of drug-free NPs led to mild Zmel cell toxicity. When assessing the interactions of NPs with Zmel cells at the chosen NP concentration of 100 μg $mL^{-1}$, we observed micron-scale clusters at the cell surface independently of DOX loading (Fig. 2B). Altogether, this suggests that highly concentrated NPs (above 50 μg $mL^{-1}$) are detrimental to Zmel tumor cells and DOX loading provides a concentration-dependent anti-tumoral beneficial effect. Notably, cell toxicity was distinctly higher for Dox_NPs than for the NPs without the drug, clearly highlighting a drug-specific cellular response.

### HSA NPs interact with the endothelium and macrophages

Probing the *in vivo* behavior of NPs is instrumental to study their interactions with the host or their circulation time, which ultimately determines the efficacy of the therapeutics. Because the size, shape, and surface features of NPs can be tuned, *in vivo* tracking is the only method that enables a clear analysis

 

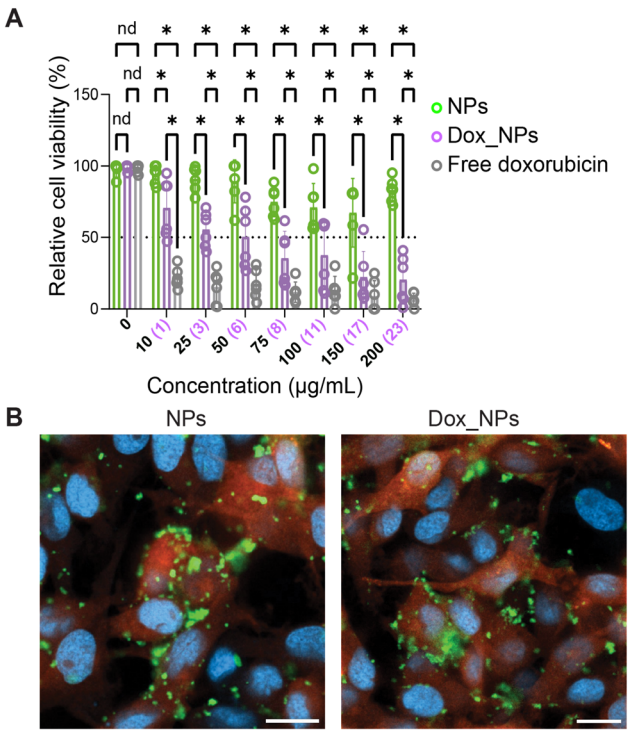


**Fig. 2** HSA NPs affect zebrafish melanoma cell viability *in vitro*. (A) Quantification of zebrafish melanoma cells' (Zmel_tdT) viability upon a 48-hour treatment with HSA NPs (with and without doxorubicin) using the crystal violet assay. Concentrations of NPs and doxorubicin loaded inside the Dox_NPs are indicated in brackets (purple). Free doxorubicin in solution was also included as a positive control. The results were normalized to untreated cells. The DOX-containing NPs (Dox_NPs) showed a dose-dependent effect similar to that of free DOX while cell viability is only affected at high NP concentrations for the NPs without the drug. The data were analyzed using two-way ANOVA followed by the two-stage linear step-up post-test procedure of Benjamini, Krieger and Yekutiel and displayed as the mean ± SD. (B) Representative images of the interactions of NPs (green) with the zebrafish melanoma (Zmel_tdT) cell line (red). The cells were exposed for 5 hours at 28 °C to 100 μg $mL^{-1}$ NPs or doxorubicin-loaded NPs, both surface-modified with HSA-FITC. DAPI stained nuclei are shown in blue. Scale bar = 10 μm.

of how these parameters control their biodistribution, preferential accumulation in specific organs, toxicity, and final fate[59–61] In this context, the zebrafish embryo has proven to be a model of choice for NP toxicity, biodistribution and drug targeting efficacy.[29,30,37]

Serum albumin nanoparticles have been extensively studied as anti-cancer drug delivery agents, due to their efficient uptake by cancer cells.[62–64] Upon uptake, the lysosomal degradation of serum albumin NPs induces cancer cell death through the release of their encapsulated drugs.[65] Among FDA-approved drugs, DOX is known for its selective tumor localization and pharmacokinetic properties, and it has been encapsulated inside nanocarriers.[66–68] Although zebrafish does not have serum albumin proteins, it has been shown that HSA can be processed in the liver of juvenile zebrafish, indicating the relevance of the model.[69] Moreover, the size of the HSA-modified NPs did not allow for direct absorption of NPs from fish water. Hence, microinjection of NPs into the blood stream was preferred and it enabled NP dissemination throughout the vasculature, which is in agreement with the biodistribution of different nanoformulations injected intravascularly.

Hence, in a first *in vivo* study, we assessed the stability and biodistribution of FITC-labeled HSA NPs (with and without DOX) in a relevant animal model and in real time. When microinjected into the duct of Cuvier of transgenic zebrafish strains Tg(Kdrl.hsa-HRAS:mCherry)[54] and Tg(mpeg1:Gal4 UAS:NTR-mCherry)[55,56] that label endothelial cells and macrophages, respectively (Fig. 3A and D), the HSA-FITC NPs disseminated throughout the embryo irrespective of the transgenic line. Regarding their interactions with the endothelial system, many NPs and Dox_NPs were found in the caudal plexus area and in the head, close to optic and other brain vessels. Furthermore, the NPs without the drug remained much longer in circulation than the Dox_NPs (found static at 3 hpi already, Fig. 3B), suggesting that the presence of DOX has an effect on the fate of these NPs in the zebrafish blood stream. Both NPs and Dox_NPs showed a similar percentage of colocalization to endothelial cells (Fig. 3C) at 3 hpi, indicating that DOX encapsulation had no distinctive effect on this phenomena. Confocal imaging confirmed that some NPs were internalized by endothelial cells independently of DOX loading. Interestingly, we noticed that Dox_NPs were more prone to spread across the extravascular space at 24 hpi (Fig. S3A and B). Dox_NPs rapidly form immobile aggregates in proximal yet extravascular regions. This suggests that Dox_NPs might interact with specific host cell types or induce cellular mechanisms that can aid their extravasation. In general, NPs are unable to escape interactions with host proteins and the consequent formation of a protein corona. This phenomenon ends up enabling their visibility to phagocytic cells.

Interestingly, the caudal plexus area homes the origin of macrophages;[70] it might thereby be possible that high accumulation of NPs in this area is due to macrophage engulfment. To confirm this hypothesis, NPs were microinjected into the zebrafish fluorescently labeled with the macrophage reporter line Tg(mpeg1:Gal4UAS:NTR-mCherry).[55,56] Upon injection, the NPs and Dox_NPs were found to be distributed throughout the embryo (Fig. 3E). At 3 hpi, the Dox_NPs were found to be colocalized with macrophages at a higher percentage than their counterparts without DOX (Fig. 3F), pointing at a potential faster clearance of Dox_NPs by macrophages. Additionally, at a later time point (24 hpi), around 35% of both NPs, with and without DOX, colocalized with macrophages (Fig. S3C), indicating that their removal from circulation at later stages in the zebrafish is similar, irrespective of the encapsulated drug. In this report, we did not address the uptake of NPs by neutrophils, as it has been shown that neutrophils are less involved than macrophages in internalizing NPs and other vesicles when administered.[22,58,71]

Hence, overall, by analyzing the colocalization between the NPs, the macrophages and the endothelium, the here-pro-

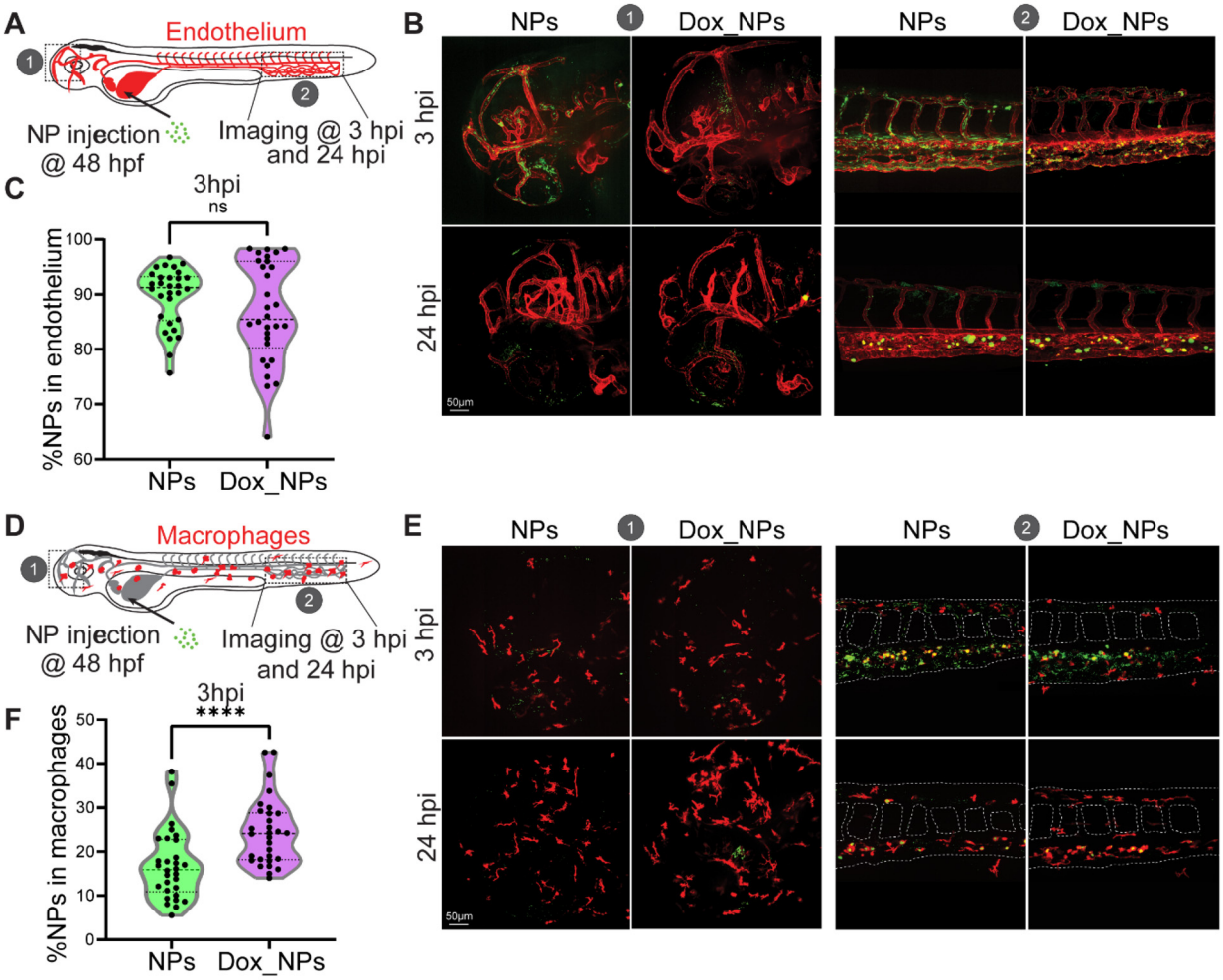


**Fig. 3** Biodistribution of HSA NPs and their interaction with endothelial cells and macrophages. (A) Description of the experimental setup: 48 hour post-fertilization (hpf), Tg(Kdrl.hsa-HRAS:mCherry) zebrafish embryos (endothelial cells in red) were injected intravascularly *via* the duct of Cuvier with both NPs and DOX-containing NPs (Dox_NPs) surface-modified with HSA-FITC. Embryos were imaged in the head (1) and caudal plexus area (2) 3 or 24 hour post-injection (hpi). Representative images (B) of the NPs in the head (1) and caudal plexus (2) areas, and quantification of the NPs colocalized with the endothelium (C). At 3 hpi, there is no difference between the NP and Dox_NP injected groups (Mann–Whitney test, 3 independent experiments, and 30 embryos in total). (D) Description of the experimental setup: 48 hour post-fertilization (hpf), Tg(mpeg-ntr:mCherry) zebrafish embryos (macrophages in red) were injected intravascularly *via* the duct of Cuvier with both NPs and DOX-containing NPs (Dox_NPs) surface-modified with HSA-FITC. Embryos were imaged in the head (1) and caudal plexus area (2) at 3 or 24 hpi. Representative images (E) of the NPs in the head (1) and caudal plexus (2) areas, and quantification of the NPs colocalized with macrophages (F). At 3 hpi, Dox_NPs exhibited significantly higher colocalization with macrophages as compared to the NPs without the drug (Mann–Whitney test, $p < 0.0001$, 3 independent experiments, and 30 embryos in total). Scale bar = 50 µm.

posed method efficiently detects most NPs injected into the system and enables the insightful quantification of NP fractions present in colocalizing regions. The elevated colocalization with macrophages, specifically at short-times after injection, can be associated with their phagocytic activity, though this remains to be fully elucidated.

### HSA NPs do not affect zebrafish vascular and innate immune embryo physiology

We further analyzed endothelial and macrophage homeostasis upon injection of NPs into 48 hpf Tg(Kdrl.hsa-HRAS:mCherry)[54] and Tg(mpeg1:Gal4UAS:NTR-mCherry)[55,56] zebrafish embryos (Fig. 4A and D). We used the length of the mesencephalic vein (MsV) and the intersomitic vessel (ISV) as a proxy for vascular homeostasis. At 24 hpi, the vessel anatomies in the head and trunk of the injected embryos had similar lengths irrespective of the injected NPs (with and without DOX, Fig. 4B and C). Similarly, at 24 hpi, the ramified shape of macrophages was maintained upon microinjection of the NPs (Fig. 4E), suggesting that there was no activation of macrophages at this time point, which can be assessed by their round shape. Hence, macrophage homeostasis at 24 hpi remained unperturbed in zebrafish injected with both NPs and Dox_NPs. Furthermore, the number of macrophages in the head and trunk was also maintained irrespective of their injection with NPs and Dox_NPs (Fig. 4F), and pacemaker

 

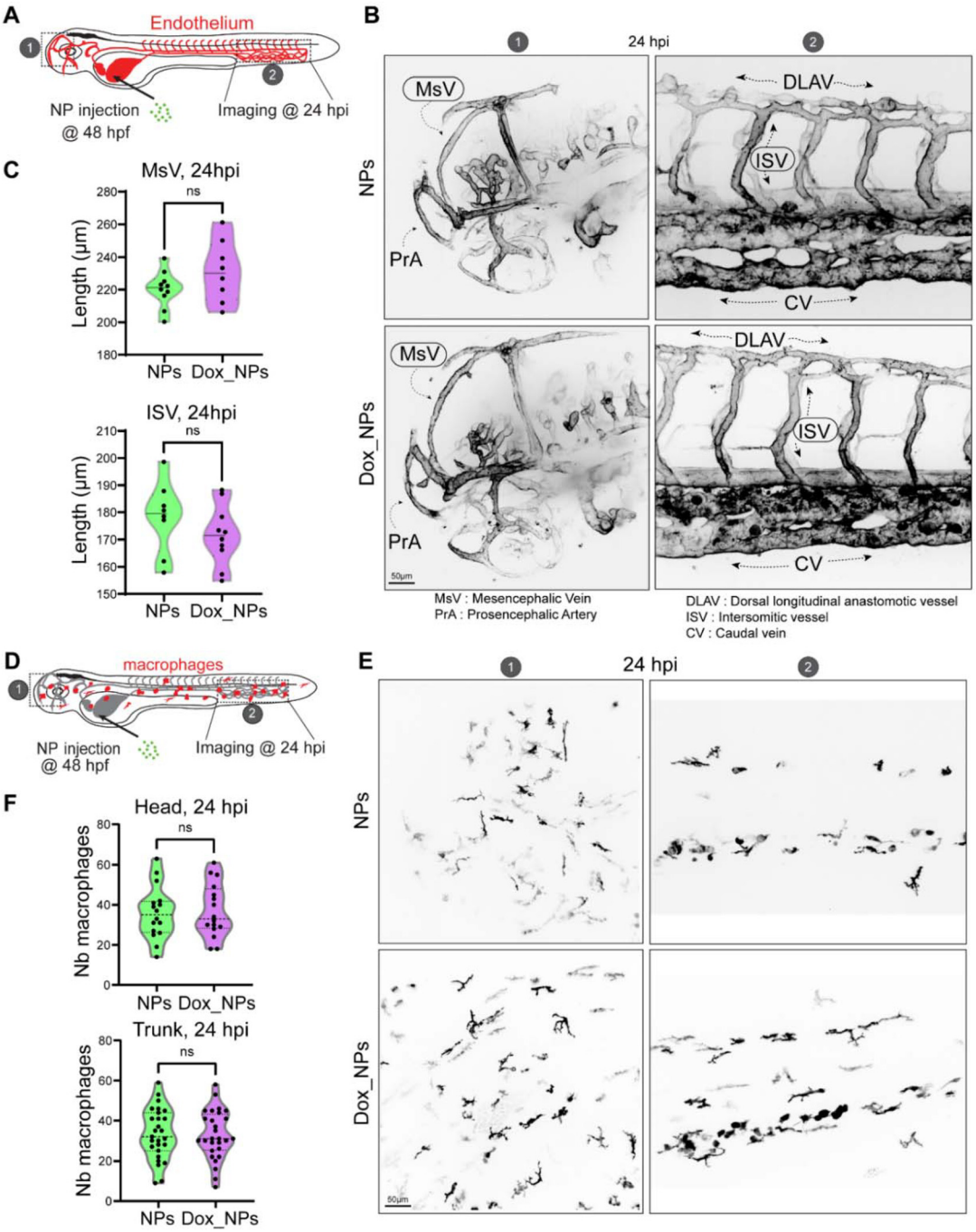


**Fig. 4** Endothelial and macrophage homeostasis remain unperturbed. (A) Description of the experimental setup: 48 hour post-fertilization (hpf), Tg (Kdrl.hsa-HRAS:mCherry) zebrafish embryos (endothelial cells in red) were injected intravascularly *via* the duct of Cuvier with both NPs and DOX-containing NPs (Dox_NPs) surface-modified with HSA-FITC. Embryos were imaged in the head (1) and caudal plexus area (2) at 24 hpi. (B) Representative images of the mesencephalic vein (MsV) in the head (1) and the intersomitic vessel (ISV) in the caudal plexus (2) at 24 hpi. (C) Quantification of MsV (upper) and ISV (lower) lengths showed no difference between the NP and Dox_NP injected groups at 24 hpi (unpaired *t* test, 3 experiments, 8 embryos for NPs, and 10 embryos for Dox_NPs). (D) Description of the experimental setup: 48 hour post-fertilization (hpf), Tg (mpeg-ntr:mCherry) zebrafish embryos (macrophages in red) were injected intravascularly *via* the duct of Cuvier with both NPs and DOX-containing NPs (Dox_NPs) surface-modified with HSA-FITC. Embryos were imaged in the head (1) and caudal plexus area (2) at 24 hpi. (E) Representative images of macrophages in the head (1) and caudal plexus areas (2) at 24 hpi. (F) Quantification of the number of macrophages at 24 hpi showed no difference between the NP and Dox_NP groups in both the head (upper) and trunk (lower) areas (unpaired *t* test, 3 independent experiments, 16 embryos per treatment in total for the head, and 27 embryos per treatment in total for the trunk). Scale bar is 50 µm.

activity was not altered (Fig. S4A). For the latter, the unperturbed heart rate in the presence of DOX is a noteworthy result given the known cardiotoxicity[68,72] of this chemotherapeutic drug.

Altogether, these data suggest that the HSA NPs, with and without DOX, after 24 hours of injection in the zebrafish blood circulation do not alter the main morphological features of the embryo (the length of main vessels, the number of macrophages, and the absence of noticeable phenotypic modifications).

### HSA NPs reduce tumor growth *in vivo* but affect survival

The zebrafish model, with its high similarity in genome with humans[73–75] (around 70%), easy manipulation and amenability for high-throughput screens, has been utilized as an effective xenotransplantation model without the risk of rejection for almost the past two decades.[23,25,26,76] Several embryonic zebrafish xenograft studies have used doxorubicin as a loaded drug in different nanoparticle formulations and have shown reduction in tumor burden.[46,48,49,67] Albeit the promising results, there are still limitations in their clinical translation partly due to their anatomical differences from mammals and due to the lack of an adaptive immune system at this developmental stage. With this in mind, we envisioned to test the HSA NPs in a zebrafish embryo model that used syngeneic zebrafish melanoma (Zmel) cells for transplantation. This cell line forms metastasis within 3 days after their injection in zebrafish embryos. We next tested whether the HSA NPs could successfully impair metastatic outgrowth in this syngeneic experimental metastasis model. First, zebrafish wild-type embryos were intravascularly injected with fluorescently-labeled zebrafish melanoma cancer cells (Zmel_tdT) at 36 hpf. This injection was followed by injections of fluorescent HSA-FITC NPs (with and without DOX) at 48 hpf (Fig. 5A). The injected embryos were longitudinally imaged and assessed at 3, 24 and 96 hpi to document metastatic outgrowth (Fig. 5B). Both the NPs and Dox_NPs reduced the metastatic outgrowth of Zmel cells (50% and 31%, respectively) (Fig. 5B and C) in comparison with the control PBS group. Unexpectedly, we observed a significant mortality of embryos 4 days post-injection, which reached 47 and 80% for the NPs and Dox_NPs, respectively (Fig. 5D). Thus, despite showing remarkable anti-metastatic potency, yet independently of DOX loading, the HSA NPs exhibited an unexpected mortality that warrants further investigation. As for any kind of chemotherapeutic, the NP dose, their unwanted interactions with other organs and tissues, and their removal pathways need to be fully screened and optimized.

Notably, the *in vitro* NP experiments with Zmel melanoma cells had already underlined the fact that the HSA NPs, with and without the drug, exhibit strong unspecific interactions with the cell membrane, resulting in NP aggregates. Indeed, for the HSA NPs, 10–20% colocalization between tumor cells and NPs was obtained at all evaluated time points (Fig. S4B), confirming potential cell–nanomaterial interactions also *in vivo*. Herein, we assume that these non-specific interactions could be behind the underlying mechanisms that inhibit or perturb cell–cell communication, a *sine qua non* condition for tumor volume progression in this metastatic model. As it has been reported in multicellular tumor spheroids, the presence of NPs during the process of spheroid formation can alter the spheroid morphology, resulting in the generation of smaller or less compact multicellular masses.[77]

### High HSA-NPs further reduce metastatic outgrowth and improve survival *in vivo*

HSA is a protein that was reported to reduce the opsonization of several types of NPs in cancer models, thereby increasing their circulation time,[78,79] and to mediate the internalization of drug payloads into tumors *via* its interaction with several receptors overexpressed in tumor cells.[80,81] With this in mind, we explored the effect of increasing the surface coverage of HSA NPs on their anti-metastatic potential. We increased the concentration of HSA immobilized on the NP surface by adding an additional HSA coating step with a 10 times more concentrated HSA protein solution as compared to the first step. This increased surface concentration of HSA from 96 (previous HSA coating) to 428 μg HSA per mg of NPs (high HSA NP coating) results in 4 times more immobilized HSA at the surface of the NPs (Fig. 6A). This effect was attributed to the IBAM grafts at the STMS surface, which allow for tight immobilization of HSA with increasing immobilized amounts as a function of the initial HSA concentrations, as previously shown by Bizeau *et al.*[51] We further assessed colloidal stability in different buffers: RPMI, PBS and HEPES by DLS (Fig. 6B–E and Fig. S5A and B). The hydrodynamic diameter in RPMI cell culture medium of the high HSA NPs with or without DOX remained similar (and even slightly better) to the corresponding HSA NPs, suggesting overall a good colloidal stability (187 ± 8 nm for high HSA NPs *versus* 170 ± 7 nm for high HSA-DOX NPs) but a micron size aggregation state in PBS or HEPES.

These high HSA NPs were administered to embryos as done for the HSA NPs. The high HSA NPs showed similar bio-distribution *in vivo* to that of HSA NPs and had no impact on the overall physiology of zebrafish embryos. When subjected to experimental metastasis, we again observed a significant reduction of metastatic outgrowth at 96 hpi for both NP types, with 69% and 53% tumor volume reduction for the NPs and Dox_NPs, respectively (Fig. 6F–H), when compared to the PBS-injected embryos. Interestingly, higher HSA coating onto the NP surface increased anti-metastatic effects up to 26% and 49% for the NPs and Dox_NPs, respectively, when compared to the HSA NPs. In a recent work with bovine serum albumin (BSA) nanoparticles (without a hard inorganic core, as here employed), Cakan-Akdogan *et al.* showed that these BSA-NPs delivered intravenously to the zebrafish larvae were able to target circulating tumor cells (CTCs) in a zebrafish xenograft model.[82] In addition, the presence of DOX encapsulated inside these BSA-NPs was related to CTC cell death. These observations are in agreement with the colocalization found in this study between Zmel cells and HSA NPs (Fig. S4B) and also with

 

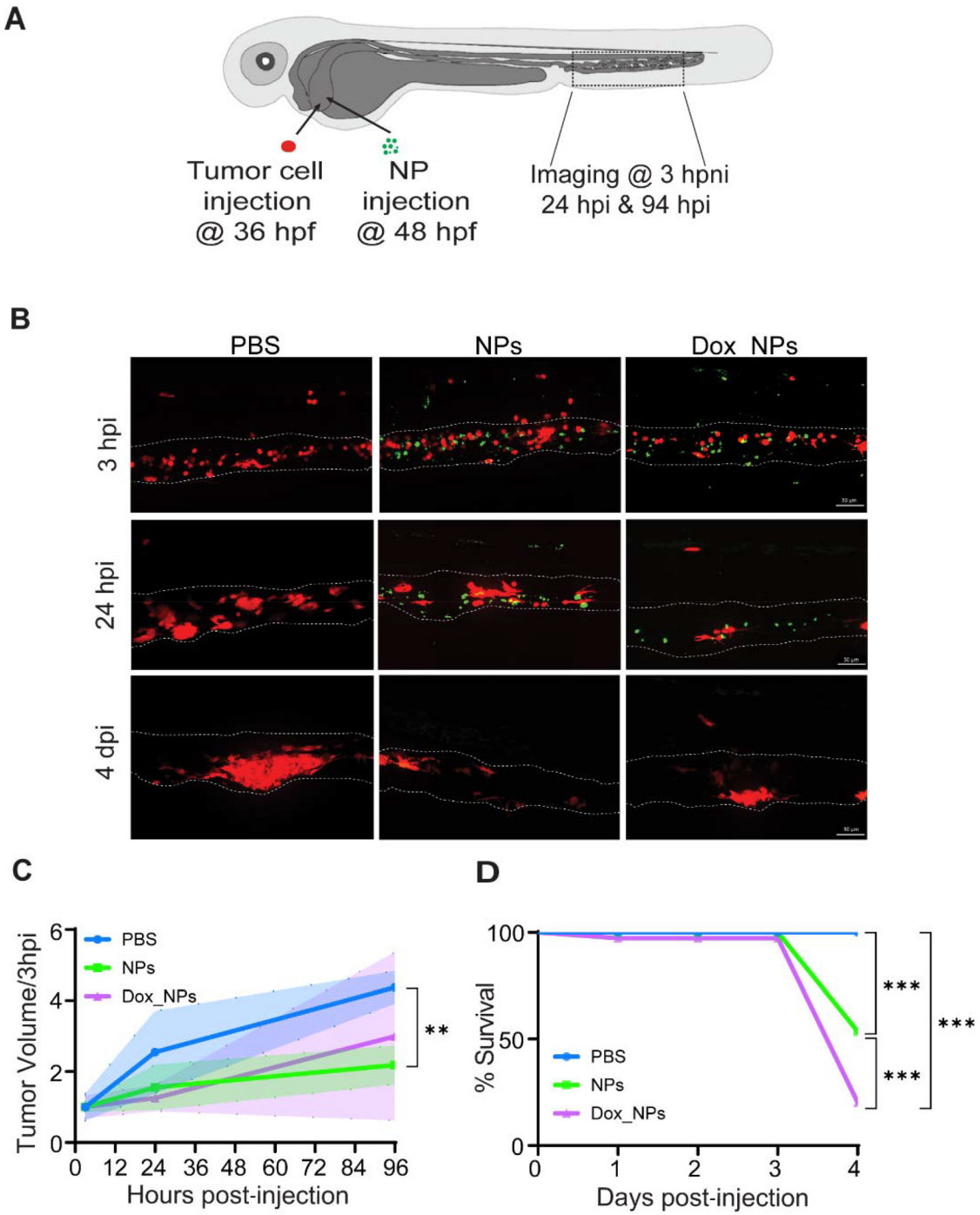


**Fig. 5** Reduction of tumor growth upon HSA NP injection. (A) Description of the experimental setup: 36 hour post-fertilization (hpf), wildtype zebrafish embryos were injected intravascularly *via* the duct of Cuvier with zebrafish melanoma cells (Zmel_tdT, in red). At 48 hpf, embryos with grafted Zmel_tdT cells were divided into three groups and injected with PBS, NPs and DOX-containing NPs (Dox_NPs), respectively. The NPs (green) were surface-modified with HSA-FITC. The caudal plexus regions were imaged at 3 h, 24 h and 96 h post-NP injection (hpi) to follow tumor growth. (B) Representative images of the caudal plexus area from engrafted embryos at 3 h, 24 h and 96 h post-injection of PBS, NPs and Dox_NPs. Scale bar is 50 μm. (C) Quantification of tumor volume using Imaris showed a substantial tumor volume reduction with the NPs and Dox_NPs at 96 hpi when compared to the PBS injected group. The data were normalized according to the initial volume at 3 hpi for each embryo (two-way ANOVA followed by the two-stage linear step-up procedure of Benjamini, Krieger and Yekutieli post-test, with $p$ = 0.0083 for the PBS/NPs, $p$ = 0.081 for the PBS/Dox_NPs, and $p$ = 0.2 for the NPs/Dox_NPs, 1 experiment, 3 embryos per group). (D) Survival analysis of tumor-grafted embryos after intravascular injections of PBS, NPs and Dox_NPs showed significant embryo mortality, indicating that the NPs are harmful to tumor-grafted embryos after day 3 post-injection (log-rank (Mantel–Cox) test with the Bonferroni post-test correction; $p$ = 0,0003 for the PBS/NPs, $p$ = 0,0003 for the PBS/Dox_NPs, and $p$ = 0.0069 for the NPs/Dox_NPs, 3 independent experiments, 27, 28 and 29 embryos in total for the PBS, NPs and Dox_NPs, respectively).

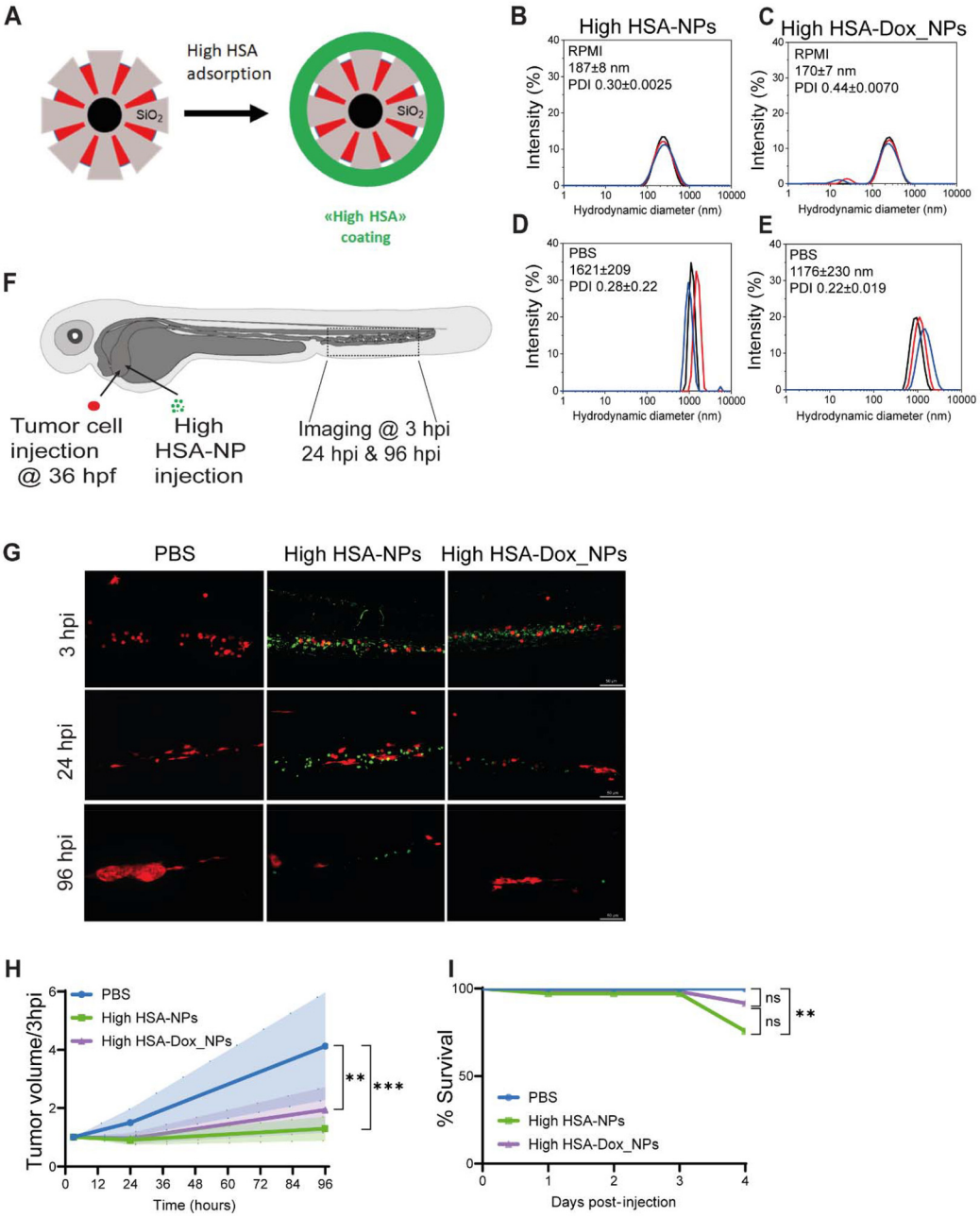


**Fig. 6** Main physicochemical features of the core–shell NPs surface-modified with high HSA and their beneficial effects on tumor reduction and reduced mortality. (A) Schematic view of HSA adsorption onto DOX-loaded NPs for high HSA NPs. As for the previous HSA NPs, the protein was immobilized on the surface after DOX loading on the mesoporous silica shell. For the high HSA NPs, the protein surface coverage is increased 4-fold. Right: dynamic light scattering of the high HSA NPs in RPMI (B and C) and PBS (D and E). DLS measurements were performed in triplicate in each medium, as indicated in the DLS graphs. The average hydrodynamic diameter of the NP distribution is indicated as an inset. (F) Description of the experimental setup: 36 hours post-fertilization (hpf), wildtype zebrafish embryos were injected intravascularly *via* the duct of Cuvier with zebrafish melanoma cells (Zmel_tdT, red). At 48 hpf, embryos with grafted Zmel_tdT cells were divided into three groups and injected with PBS, high HSA NPs and high HSA-Dox NPs. The NPs (green) were surface-modified with high HSA-FITC. The caudal plexus regions were imaged at 3 h, 24 h and 96 h post-NP injection (hpi) to follow tumor growth. (G) Representative images of the caudal plexus area from engrafted embryos at 3 h, 24 h and 96 h post-PBS, high HSA NP and high HSA-Dox NP injection. (H) Quantification of tumor volume using Imaris showed a significant reduction of tumor volume with high HSA NPs and high HSA-Dox NPs at 96 hpi when compared to the PBS-injected group. The data were normalized according to the initial volume at 3 hpi for each embryo (two-way ANOVA followed by the two-stage linear step-up procedure of Benjamini, Krieger and Yekutieli post-test, with $p$ = 0.0004 for the PBS/NPs, $p$ = 0.0013 for the PBS/Dox_NPs, and $p$ = 0.115 for the NPs/Dox_NPs, 1 experiment, 3 embryos per group). (I) Survival analysis of tumor-grafted embryos after intravascular injection of PBS, high HSA NPs and high HSA-Dox NPs showed improved survival efficacy compared to the previous HSA NPs (log-rank (Mantel–Cox) test with the Bonferroni post-test correction, with $p$ = 0.003 for the PBS/NPs, $p$ = 0.125 for the PBS/Dox_NPs, and $p$ = 0.324 for the NPs/Dox_NPs, $p$ = 3 independent experiments, 31, 30 and 32 embryos in total for the PBS, NPs and Dox_NPs, respectively).

the dampening in tumor progression upon treatment with the NPs. As HSA is known to activate the innate immune system through Toll-like receptor 4 (TLR4) and induce inflammation,[83–87] and also as observed in Fig. S3C, where approximately 35% of the NPs were internalized by macrophages at 24 hpi, we speculate that the HSA-coated NPs may activate a prompt immune response that leads to effective NP internalization and removal from circulation.

Notably, these high HSA NPs enabled a significant gain in survival at 4 dpi in the tumor-grafted zebrafish (with and without DOX, Fig. 6I), that puts them close to the control injected with PBS. In comparison with Doxil, the only FDA-approved nanoparticle formulation containing doxorubicin, our Dox_NPs exhibit improved safety in zebrafish. Doxil has been reported to induce 50% mortality of zebrafish at 72 hpi after exposure to 0.2 mg $mL^{-1}$ of Doxil directly suspended in the zebrafish medium, whereas our high-HSA Dox_NPs or NPs produce only a minor reduction in survival following direct intravenous injection at 0.5 mg $mL^{-1}$ at 96 hpi.

Altogether, these results suggest that (i) the HSA NPs impair metastatic outgrowth independently of the presence of encapsulated DOX and that (ii) increasing the HSA coverage of NPs improves both the reduction in tumor volume and the overall survival of embryos. Here, the size and the mere presence of the NPs in circulation, their aggregation at short times in biological media, and their strong interactions with the endothelium *in vivo*, and with the Zmel cells *in vitro* and also *in vivo*, might altogether contribute to the anti-tumoral effects observed. Nevertheless, the specific biological pathways and mechanisms behind the here-observed reduction in tumor outgrowth remain to be elucidated.

## Conclusion

Altogether, the results of this study confirm the suitability and biosafety of HSA-coated IO STMS core–shell NPs and their therapeutic efficacy in a syngeneic zebrafish melanoma model. The outgrowth of the metastatic foci was markedly halted when the HSA-coated NPs were intravascularly injected in the zebrafish embryos pre-inoculated with melanoma cells (13.9 ng of NPs and 1.57 ng of DOX injected). This anti-metastatic effect was evidenced regardless of the encapsulated drug. By increasing the amount of HSA immobilized on the NPs, a significant improvement was observed in the anti-tumoral effect and also in the overall survival of the xenografted animals. The core–shell nanoparticles surface-modified with high HSA appear therefore as promising nanovehicles for drug encapsulation, fertile interactions with tumoral cells, tumor targeting and localized magnetic/NIR hyperthermia treatments.

## Conflicts of interest

The authors declare that they have no conflicts of interest.

## Abbreviations

| | |
|---|---|
| NPs | Nanoparticles |
| IO@STMS | Iron oxide@stellate mesoporous silica |
| MSNs | Mesoporous silica nanoparticles |
| SPIONs | Superparamagnetic iron oxide nanoparticles |
| GMP | Good manufacturing practices |
| HSA | Human serum albumin |
| DOX | Doxorubicin |
| DLS | Dynamic light scattering |
| TEM | Transmission electron microscopy |
| TAMRA | Tetramethylrhodamine (fluorescent dye) |
| DMEM | Dulbecco's modified Eagle's medium |
| FBS | Fetal bovine serum |
| PBS | Phosphate-buffered saline |
| MTT | [3-(4,5-Dimethylthiazol-2-yl)-2,5-diphenyltetrazolium bromide] cell viability assay |
| hpf | Hours post-fertilization |
| E3 medium | Embryo medium (zebrafish culture medium) |
| MS-222 | Tricaine methanesulfonate (anesthetic) |
| S.C. | Subcutaneous |
| IC50 | Half maximal inhibitory concentration |
| PEG | Polyethylene glycol |
| MRI | Magnetic resonance imaging |
| I.V. | Intravenous |
| H&E | Hematoxylin & eosin (histological staining) |
| RNA seq | RNA sequencing |
| TLR4 | Toll-like receptor 4 |

## Data availability

Data for this article are available at Recherche.Data.Gouv repository at the https://doi.org/10.57745/Q6YRKM.

Supplementary information (SI) is available. See DOI: https://doi.org/10.1039/d5nr02444g.

## Acknowledgements

We thank all members of the Tumor Biomechanics Lab for their constant and helpful discussions throughout this investigation. We thank Pascal Kessler (PICSTRA, CRBS) for assistance in imaging and image analysis and the members of the Department of Chemistry of Inorganic Materials Chemistry (DCMI) for their assistance with nanoparticle synthesis. D. M. and S. H. acknowledge the Canceropole Est (project VIVIRMAG) for financial support. The transmission electron microscopy platform of the IPCMS is acknowledged for technical support. MT thanks the University of Strasbourg, the National Scientific and Technical Research Council (CONICET), and the Ministry of Science, Technology and Innovation (Mincyt) for financial support. We are particularly grateful to Florent Colin, who was pivotal in many parts of this study. Work and people in the Tumor Biomechanics Lab are mostly supported by the INCa (Institut National Du Cancer,

French National Cancer Institute), charities (La Ligue contre le Cancer, ARC (Association pour la Recherche contre le Cancer), FRM (Fondation pour la Recherche Médicale)), the National Plan Cancer initiative, the Region Grand Est, INSERM, the University of Strasbourg and local donators (TDLR, Club Féminin Lampertheim). This work was directly funded by the Canceropole Grand-Est, with additional support from INCa. VM was funded by ARC.

## References

1 B. Pelaz, *et al.*, in *Nano Focus Diverse Applications of Nanomedicine*, 2017. DOI: 10.1021/acsnano.6b06040.
2 F. Torres Andón and B. Fadeel, Nanotoxicology: Towards Safety by Design, *in*, 2014, 391–424, DOI: 10.1007/978-3-319-08084-0_14.
3 T. Sun, *et al.*, Engineered nanoparticles for drug delivery in cancer therapy, *Angew. Chem., Int. Ed.*, 2014, **53**, 12320–12364.
4 T. I. Janjua, Y. Cao, C. Yu and A. Popat, Clinical translation of silica nanoparticles, *Nat. Rev. Mater.*, 2021, **6**, 1072–1074.
5 V. Mamaeva, C. Sahlgren and M. Lindén, Mesoporous silica nanoparticles in medicine—Recent advances, *Adv. Drug Delivery Rev.*, 2013, **65**, 689–702.
6 S.-H. Wu, C.-Y. Mou and H.-P. Lin, Synthesis of mesoporous silica nanoparticles, *Chem. Soc. Rev.*, 2013, **42**, 3862–3875.
7 M. Vallet-Regí, F. Schüth, D. Lozano, M. Colilla and M. Manzano, Engineering mesoporous silica nanoparticles for drug delivery: where are we after two decades?, *Chem. Soc. Rev.*, 2022, **51**, 5365–5451.
8 J. G. Croissant, Y. Fatieiev and N. M. Khashab, Degradability and Clearance of Silicon, Organosilica, Silsesquioxane, Silica Mixed Oxide, and Mesoporous Silica Nanoparticles, *Adv. Mater.*, 2017, **29**, 1604634.
9 A. Adam, *et al.*, Orienting the Pore Morphology of Core-Shell Magnetic Mesoporous Silica with the Sol-Gel Temperature, Influence on MRI and Magnetic Hyperthermia Properties, *Molecules*, 2021, **26**, 971.
10 F. Perton, *et al.*, Fluorescent and Magnetic Stellate Mesoporous Silica for Bimodal Imaging and Magnetic Hyperthermia, *Appl. Mater. Today*, 2019, **16**, 301–314.
11 A. Adam, *et al.*, Core-shell iron oxide@stellate mesoporous silica for combined near-infrared photothermia and drug delivery: Influence of pH and surface chemistry, *Colloids Surf., A*, 2022, **640**, 128407.
12 F. Fenaroli, *et al.*, Nanoparticles as Drug Delivery System against Tuberculosis in Zebrafish Embryos: Direct Visualization and Treatment, *ACS Nano*, 2014, **8**, 7014–7026.
13 X.-Y. Jiang, *et al.*, Quantum dot interactions and flow effects in angiogenic zebrafish (Danio rerio) vessels and human endothelial cells, *Nanomedicine*, 2017, **13**, 999–1010.
14 C. Chakraborty, A. R. Sharma, G. Sharma and S. S. Lee, Zebrafish : A complete animal model to enumerate the nanoparticle toxicity, *J. Nanobiotechnol.*, 2016, 1–13, DOI: 10.1186/s12951-016-0217-6.
15 S. Lin, Y. Zhao, A. E. Nel and S. Lin, Zebrafsh: An In Vivo Model for Nano EHS Studies, *Small*, 2013, **9**, 1608–1618.
16 R. A. Nadar, N. Asokan, A. Curci, A. Barbanente, L. Schlatt, M. Iafisco, N. Margiotta, M. Brand, J. J. J. P. van den Beucken and S. C. G. Leeuwenburgh, Preclinical Evaluation of Platinum-Loaded Hydroxyapatite Nanoparticles in an embryonic zebrafish xenograft model Preclinical evaluation of platinum-loaded hydroxyapatite nanoparticles in an embryonic zebra fi sh xenograft model, *Nanoscale*, 2020, **12**, 13582–13594.
17 L. Evensen, *et al.*, Zebrafish as a model system for characterization of nanoparticles against cancer, *Nanoscale*, 2016, **8**, 862–877.
18 S. Sieber, *et al.*, Zebrafish as an early stage screening tool to study the systemic circulation of nanoparticulate drug delivery systems in vivo, *J. Controlled Release*, 2017, **264**, 180–191.
19 S.-K. Ko, X. Chen, J. Yoon and I. Shin, Zebrafish as a good vertebrate model for molecular imaging using fluorescent probes, *Chem. Soc. Rev.*, 2011, **40**, 2120–2130.
20 N.-J. K. Dal, *et al.*, Zebrafish Embryos Allow Prediction of Nanoparticle Circulation Times in Mice and Facilitate Quantification of Nanoparticle–Cell Interactions, *Small*, 2020, **16**, 1906719.
21 P. L. Johansen, F. Fenaroli, L. Evensen, G. Griffiths and G. Koster, Optical micromanipulation of nanoparticles and cells inside living zebrafish, *Nat. Commun.*, 2016, 1–8, DOI: 10.1038/ncomms10974.
22 F. Fenaroli, *et al.*, Nanoparticles as Drug Delivery System against Tuberculosis in Zebrafish Embryos: Direct Visualization and Treatment, *ACS Nano*, 2014, **8**, 7014–7026.
23 M. Haldi, C. Ton, W. L. Seng and P. McGrath, Human melanoma cells transplanted into zebrafish proliferate, migrate, produce melanin, form masses and stimulate angiogenesis in zebrafish, *Angiogenesis*, 2006, **9**, 139–151.
24 M. Konantz, *et al.*, Zebrafish xenografts as a tool for in vivo studies on human cancer, *Ann. N. Y. Acad. Sci.*, 2012, **1266**, 124–137.
25 N. Asokan, *et al.*, Long-term in vivo imaging reveals tumor-specific dissemination and captures host tumor interaction in zebrafish xenografts, *Sci. Rep.*, 2020, **10**, 1–14.
26 M. Tavares Barroso, *et al.*, Establishment of Pancreatobiliary Cancer Zebrafish Avatars for Chemotherapy Screening, *Cells*, 2021, **10**, 2077.
27 E. van Rooijen, M. Fazio and L. Zon, I. From fish bowl to bedside: The power of zebrafish to unravel melanoma pathogenesis and discover new therapeutics, *Pigm. Cell Melanoma Res.*, 2017, **30**, 402–412.
28 A. Kocere, *et al.*, Real-time imaging of polymersome nanoparticles in zebrafish embryos engrafted with melanoma

 

cancer cells: Localization, toxicity and treatment analysis, *EBioMedicine*, 2020, **58**, 102902.
29 E. Haque and A. C. Ward, Zebrafish as a Model to Evaluate Nanoparticle Toxicity, *Nanomaterials*, 2018, **8**, 561.
30 P. V. Asharani, Y. Lian Wu, Z. Gong and S. Valiyaveettil, Toxicity of silver nanoparticles in zebrafish models, *Nanotechnology*, 2008, **19**, 255102.
31 J. Mal, *et al.*, A comparison of fate and toxicity of selenite, biogenically, and chemically synthesized selenium nanoparticles to zebrafish (Danio rerio) embryogenesis, *Nanotoxicology*, 2017, **11**, 87–97.
32 P. Bonfanti, *et al.*, Functional silver-based nanomaterials affecting zebrafish development: the adverse outcomes in relation to the nanoparticle physical and chemical structure, *Environ. Sci.: Nano*, 2024, **11**, 2521–2540.
33 C. Mutalik, *et al.*, Zebrafish Insights into Nanomaterial Toxicity: A Focused Exploration on Metallic, Metal Oxide, Semiconductor, and Mixed-Metal Nanoparticles, *Int. J. Mol. Sci.*, 2024, **25**, 1926.
34 P. Nadrah, *et al.*, Hindered Disulfide Bonds to Regulate Release Rate of Model Drug from Mesoporous Silica, *ACS Appl. Mater. Interfaces*, 2013, **5**, 3908–3915.
35 N. Velikova, *et al.*, Broadening the antibacterial spectrum of histidine kinase autophosphorylation inhibitors via the use of ε-poly-L-lysine capped mesoporous silica-based nanoparticles, *Nanomedicine*, 2017, **13**, 569–581.
36 I. Paatero, *et al.*, Analyses in zebrafish embryos reveal that nanotoxicity profiles are dependent on surface-functionalization controlled penetrance of biological membranes, *Sci. Rep.*, 2017, **7**, 8423.
37 F. Sharif, F. Porta, A. H. Meijer, A. Kros and M. K. Richardson, Mesoporous silica nanoparticles as a compound delivery system in zebrafish embryos, *Int. J. Nanomed.*, 2012, **7**, 1875–1890.
38 G. K. Nasrallah, *et al.*, A systematic investigation of the biotoxicity of core-shell magnetic mesoporous silica microspheres using zebrafish model, *Microporous Mesoporous Mater.*, 2018, **265**, 195–201.
39 T.-P. Liu, S.-H. Wu, Y.-P. Chen, C.-M. Chou and C.-T. Chen, Biosafety evaluations of well-dispersed mesoporous silica nanoparticles: towards in vivo-relevant conditions, *Nanoscale*, 2015, **7**, 6471–6480.
40 J. M. Brown, L. Recht and S. Strober, The Promise of Targeting Macrophages in Cancer Therapy, *Clin. Cancer Res.*, 2017, **23**, 3241–3250.
41 A. R. Poh and M. Ernst, Targeting Macrophages in Cancer: From Bench to Bedside, *Front. Oncol.*, 2018, **8**, 49.
42 L. Pang, *et al.*, Exploiting macrophages as targeted carrier to guide nanoparticles into glioma, *Oncotarget*, 2016, **7**, 37081–37091.
43 S. K. Patel and J. M. Janjic, Macrophage targeted theranostics as personalized nanomedicine strategies for inflammatory diseases, *Theranostics*, 2015, **5**, 150–172.
44 P. Zhao, *et al.*, Dual-Targeting to Cancer Cells and M2 Macrophages via Biomimetic Delivery of Mannosylated Albumin Nanoparticles for Drug-Resistant Cancer Therapy, *Adv. Funct. Mater.*, 2017, **27**, 1700403.
45 Z. Xie, *et al.*, Targeting tumor hypoxia with stimulus-responsive nanocarriers in overcoming drug resistance and monitoring anticancer efficacy, *Acta Biomater.*, 2018, **71**, 351–362.
46 A. Van Driessche, *et al.*, pH-Sensitive Hydrazone-Linked Doxorubicin Nanogels via Polymeric-Activated Ester Scaffolds: Synthesis, Assembly, and In Vitro and In Vivo Evaluation in Tumor-Bearing Zebrafish, *Chem. Mater.*, 2018, **30**, 8587–8596.
47 G. Cakan-Akdogan, E. Ersoz, S. C. Sozer and E. Gelinci, An in vivo zebrafish model reveals circulating tumor cell targeting capacity of serum albumin nanoparticles, *J. Drug Delivery Sci. Technol.*, 2022, **75**, 103658.
48 S. Bozzer, *et al.*, Zebrafish: A Useful Animal Model for the Characterization of Drug-Loaded Polymeric NPs, *Biomedicines*, 2022, **10**, 2252.
49 A. Kocere, *et al.*, Real-time imaging of polymersome nanoparticles in zebrafish embryos engrafted with melanoma cancer cells: Localization, toxicity and treatment analysis, *EBioMedicine*, 2020, **58**, 102902.
50 J. Bizeau, *et al.*, Tailoring the pore structure of iron oxide core@stellate mesoporous silica shell nanocomposites: effects on MRI and magnetic hyperthermia properties and applicability to anti-cancer therapies, *Nanoscale*, 2024, **16**, 15585–15614.
51 J. Bizeau, *et al.*, Protein sustained release from isobutyramide-grafted stellate mesoporous silica nanoparticles, *Int. J. Pharm.: X*, 2022, **4**, 100130.
52 E. Papini, R. Tavano and F. Mancin, Opsonins and Dysopsonins of Nanoparticles: Facts, Concepts, and Methodological Guidelines, *Front. Immunol.*, 2020, **11**, 567365.
53 D. E. Owens and N. A. Peppas, Opsonization, biodistribution, and pharmacokinetics of polymeric nanoparticles, *Int. J. Pharm.*, 2006, **307**, 93–102.
54 N. C. Chi, *et al.*, Foxn4 directly regulates, *Genes Dev.*, 2008, 734–739, DOI: 10.1101/gad.1629408.734.
55 F. Ellett, L. Pase, J. W. Hayman, A. Andrianopoulos and G. J. Lieschke, Mpeg1 Promoter Transgenes Direct Macrophage-Lineage Expression in Zebrafish, *Blood*, 2011, **117**, e49–e56.
56 J. M. Davison, *et al.*, Transactivation from Gal4-VP16 transgenic insertions for tissue-specific cell labeling and ablation in zebrafish, *Dev. Biol.*, 2007, **304**, 811–824.
57 B. Mary, S. Ghoroghi, V. Hyenne and J. G. Goetz, Live tracking of extracellular vesicles in larval zebrafish, in *Methods in Enzymology*, 2020. DOI: 10.1016/bs.mie.2020.07.013.
58 V. Hyenne, *et al.*, Studying the Fate of Tumor Extracellular Vesicles at High Spatiotemporal Resolution Using the Zebrafish Embryo, *Dev. Cell*, 2019, **48**, 554–572.
59 X. Duan and Y. Li, Physicochemical characteristics of nanoparticles affect circulation, biodistribution, cellular internalization, and trafficking, *Small*, 2013, **9**, 1521–1532.

60 E. Blanco, H. Shen and M. Ferrari, Principles of nanoparticle design for overcoming biological barriers to drug delivery, *Nat. Biotechnol.*, 2015, **33**, 941–951.
61 A. Pensado-López, *et al.*, Zebrafish Models for the Safety and Therapeutic Testing of Nanoparticles with a Focus on Macrophages, *Nanomaterials*, 2021, **11**, 1784.
62 H. Maeda, The enhanced permeability and retention (EPR) effect in tumor vasculature: the key role of tumor-selective macromolecular drug targeting, *Adv. Enzyme Regul.*, 2001, **41**, 189–207.
63 B. Demirkurt, G. Cakan-Akdogan and Y. Akdogan, Preparation of albumin nanoparticles in water-in-ionic liquid microemulsions, *J. Mol. Liq.*, 2019, **295**, 111713.
64 N. Desai, *et al.*, Increased antitumor activity, intratumor paclitaxel concentrations, and endothelial cell transport of cremophor-free, albumin-bound paclitaxel, ABI-007, compared with cremophor-based paclitaxel, *Clin. Cancer Res.*, 2006, **12**, 1317–1324.
65 P. Ma and R. J. Mumper, Paclitaxel Nano-Delivery Systems: A Comprehensive Review, *J. Nanomed. Nanotechnol.*, 2013, **4**, 1000164.
66 Z. Xie, *et al.*, Targeting tumor hypoxia with stimulus-responsive nanocarriers in overcoming drug resistance and monitoring anticancer efficacy, *Acta Biomater.*, 2018, **71**, 351–362.
67 G. Cakan-Akdogan, E. Ersoz, S. C. Sozer and E. Gelinci, An in vivo zebrafish model reveals circulating tumor cell targeting capacity of serum albumin nanoparticles, *J. Drug Delivery Sci. Technol.*, 2022, **75**, 103658.
68 O. Tacar, P. Sriamornsak and C. R. Dass, Doxorubicin: an update on anticancer molecular action, toxicity and novel drug delivery systems, *J. Pharm. Pharmacol.*, 2013, **65**, 157–170.
69 D. Cheng, M. Morsch, G. J. Shami, R. S. Chung and F. Braet, Albumin uptake and distribution in the zebrafish liver as observed via correlative imaging, *Exp. Cell Res.*, 2019, **374**, 162–171.
70 R. M. Warga, D. A. Kane and R. K. Ho, Fate mapping embryonic blood in zebrafish: multi- and unipotential lineages are segregated at gastrulation, *Dev. Cell*, 2009, **16**, 744–755.
71 L. S. Ulanova, *et al.*, Treatment of Francisella infections via PLGA- and lipid-based nanoparticle delivery of antibiotics in a zebrafish model, *Dis. Aquat. Org.*, 2017, **125**, 19–29.
72 D. Cardinale, F. Iacopo and C. M. Cipolla, Cardiotoxicity of Anthracyclines, *Front. Cardiovasc. Med.*, 2020, **7**, 26.
73 J. Etchin, J. P. Kanki and A. T. Look, Zebrafish as a Model for the Study of Human Cancer, *Methods Cell Biol.*, 2011, **105**, 309–337.
74 S. H. Lam, *et al.*, Conservation of gene expression signatures between zebrafish and human liver tumors and tumor progression, *Nat. Biotechnol.*, 2006, **24**, 73–75.
75 T. S. P. Rothenbücher, *et al.*, Zebrafish embryo as a replacement model for initial biocompatibility studies of biomaterials and drug delivery systems, *Acta Biomater.*, 2019, **100**, 235–243.
76 S. Nicoli, D. Ribatti, F. Cotelli and M. Presta, Mammalian Tumor Xenografts Induce Neovascularization in Zebrafish Embryos Mammalian Tumor Xenografts Induce Neovascularization in Zebrafish Embryos, *Cancer Res.*, 2007, 2927–2931.
77 F. Sambale, *et al.*, Three dimensional spheroid cell culture for nanoparticle safety testing, *J. Biotechnol.*, 2015, **205**, 120–129.
78 Q. Peng, *et al.*, Preformed albumin corona, a protective coating for nanoparticles based drug delivery system, *Biomaterials*, 2013, **34**, 8521–8530.
79 K. Bolaños, M. J. Kogan and E. Araya, Capping gold nanoparticles with albumin to improve their biomedical properties, *Int. J. Nanomed.*, 2019, **14**, 6387–6406.
80 A. Spada, J. Emami, J. A. Tuszynski and A. Lavasanifar, The Uniqueness of Albumin as a Carrier in Nanodrug Delivery, *Mol. Pharm.*, 2021, **18**, 1862–1894.
81 B. Elsadek and F. Kratz, Impact of albumin on drug delivery–new applications on the horizon, *J. Controlled Release*, 2012, **157**, 4–28.
82 G. Cakan-Akdogan, E. Ersoz, S. C. Sozer and E. Gelinci, An in vivo zebrafish model reveals circulating tumor cell targeting capacity of serum albumin nanoparticles, *J. Drug Delivery Sci. Technol.*, 2022, **75**, 103658.
83 V. Arroyo, R. García-Martinez and X. Salvatella, Human serum albumin, systemic inflammation, and cirrhosis, *J. Hepatol.*, 2014, **61**, 396–407.
84 S. A. David, P. Balaram and V. I. Mathan, Characterization of the interaction of lipid A and lipopolysaccharide with human serum albumin: implications for an endotoxin carrier function for albumin, *J. Endotoxin Res.*, 1995, **2**, 99–106.
85 R. Dziarski, Cell-bound albumin is the 70 kDa peptidoglycan-, lipopolysaccharide-, and lipoteichoic acid-binding protein on lymphocytes and macrophages, *J. Biol. Chem.*, 1994, **269**, 20431–20436.
86 H. Fukui, Relation of endotoxin, endotoxin binding proteins and macrophages to severe alcoholic liver injury and multiple organ failure, *Alcohol.: Clin. Exp. Res.*, 2005, **29**, 172S–179S.
87 G. Jürgens, *et al.*, Investigation into the interaction of recombinant human serum albumin with Re-lipopolysaccharide and lipid A, *J. Endotoxin Res.*, 2002, **8**, 115–126.